



ELSEVIER

Available online at www.sciencedirect.com

SCIENCE @ DIRECT®

Coastal Engineering xx (2005) xxx – xxx

**Coastal
Engineering**
 An International Journal for Coastal,
 Harbour and Offshore Engineers
www.elsevier.com/locate/coastaleng

Simulating offshore sand waves

 A.A. Németh ^{a,*}, S.J.M.H. Hulscher ^a, R.M.J. Van Damme ^b
^a Department of Civil Engineering, University of Twente, P.O. BOX 217, 7500 AE Enschede, the Netherlands

^b Department of Applied Mathematics, University of Twente, P.O. BOX 217, 7500 AE Enschede, the Netherlands

Abstract

Sand waves form a prominent regular pattern in the offshore seabeds of sandy shallow seas and pose a threat to a range of offshore activities. A two-dimensional vertical (2DV) flow and morphological simulation model describing the behaviour of these sand waves has been developed. The simulation model contains the 2DV shallow water equations, with a free water surface and a general bed load formula. The water movement is coupled to the sediment transport equation with a seabed evolution equation. The domain is non-periodic in both directions. The spatial discretisation is performed by a spectral method based on Chebyshev polynomials. A fully implicit method is chosen for the discretisation in time. Firstly, we validate the simulation model mathematically by reproducing the results obtained using a linear stability analysis for infinitely small sand waves. Hereby, we investigate a steady current situation induced by a wind stress applied at the sea surface. The bed forms we find have wavelengths in the order of hundreds of metres when the resistance at the seabed is relatively large. The results show that it is possible to model the initial evolution of sand waves with a numerical simulation model. This paper forms the necessary first step to investigate the intermediate term behaviour of sand waves.

© 2005 Published by Elsevier B.V.

Keywords: Stability analysis; Numerical analysis; Spectral method; Sand waves; Generation; Shelf seas; 2DV

1. Introduction

Large parts of shallow seas—such as the North Sea—are covered with bed features having a variety of spatial dimensions (Fig. 1). Sand waves form a prominent bed pattern with a crest to crest spacing of hundreds of metres. Sand waves are observed at water depths in the order of 30 m and their heights can reach up to several metres. The crests are often assumed oriented perpendicularly to the principal current (Johnson et al., 1981; Langhorne, 1981). Based on a theoretical analysis, Hulscher (1996) showed that sand wave crests may deviate up to 10° anti-clockwise perpendicularly from the principal direction of the current on the northern hemisphere.

An analysis of the sand market Peters et al. (2001) showed that a shortage of sand is expected in the future in the Netherlands. The crests of sand waves are assumed to have the

best composition for use in concrete. Knaapen and Hulscher (2002) showed that when a sand wave is dredged, it is able to recover in only a matter of years. This implies that small scale sand mining can be of a temporary nature only. Moreover, the behaviour of sand waves plays an important role in the selection of areas for large-scale sand extraction pits and their design. The influence of a pit or artificial island on its surrounding bed topography (including sand waves) is still unclear. Besides, the presence of sand waves changes the hydrodynamics and therefore the recolonization possibilities of benthic fauna Stolk (2000). Observations suggest that sand waves are dynamic (see for instance Allen, 1980b; Lanckneus and De Moor, 1991; Morelissen et al., 2003) and may migrate with speeds of up to several metres per year, which may cause buried pipelines to become exposed (Fig. 1). Therefore, insight into the behaviour of these sand waves is crucial to enable cost-effective management practices.

Huthnance (1982) was the first to look at a system consisting of depth-averaged tidal flow and an erodible seabed using a linear stability analysis. Within this framework, it is possible to investigate whether certain regular patterns develop as free instabilities of the system. Unstable modes comparable

* Corresponding author. Current address: Witteveen+Bos, P.O. Box 233, 7400 AE Deventer, the Netherlands.

E-mail addresses: a.nemeth@witbo.nl (A.A. Németh), s.j.m.h.hulscher@utwente.nl (S.J.M.H. Hulscher), r.m.j.vandamme@utwente.nl (R.M.J. Van Damme).

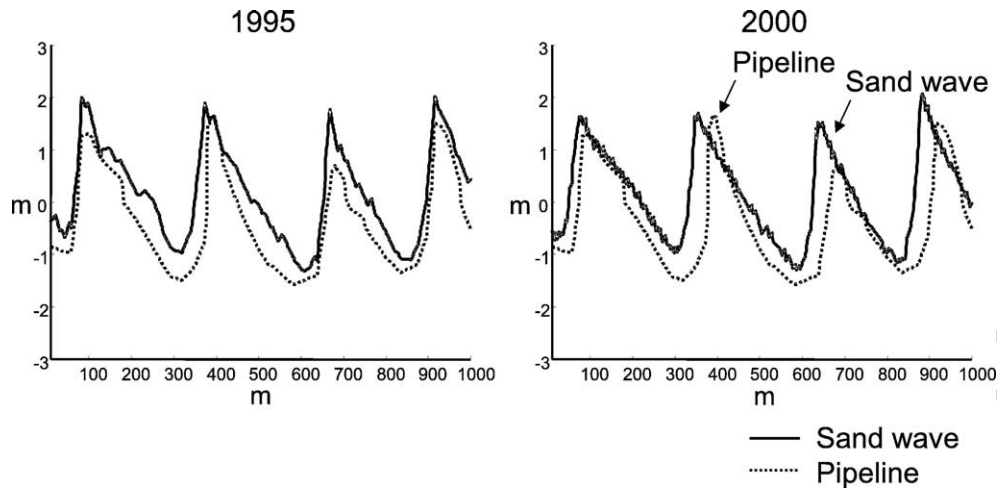


Fig. 1. Sand wave migration and pipelines. The solid line denotes the position of the seabed. The dotted line shows the position of the estimated pipeline. The measurements for two years (1995 and 2000) are shown. We can see that the sand wave is migrating to the left here, thereby exposing the buried pipeline (Courtesy Holland Offshore Consulting and State Supervision of Mines).

59 to tidal sandbanks were found, whereas smaller modes
 60 corresponding to sand waves were not initiated. This work
 61 was extended by Hulscher (1996) using a model allowing for
 62 vertical circulations and found formation of sand waves based
 63 on a horizontally averaged symmetrical tidal motion. The work
 64 showed that net convergence of sand can occur at the top of the
 65 sand waves over an entire tidal cycle (M2 tidal motion) (see
 66 also Gerkema, 2000; Komarova and Hulscher, 2000). Németh
 67 et al. (2002) extended the previous work by including an
 68 asymmetric basic flow (M0), inducing sand wave migration.
 69 Furthermore, Besio et al. (2003, 2004) discussed the effect
 70 using a stability analysis of an M4 tidal constituent on top of
 71 the M0 and M2 components.

72 A consequence of linear stability analyses is that their
 73 validity is limited to small-amplitude sand waves. However,
 74 this is far from the final aim, which is understanding the entire
 75 evolutionary process of sand wave formation. Komarova and
 76 Newell (2000) have extended the linear analysis by Komarova
 77 and Hulscher (2000) into the weakly non-linear regime for
 78 investigation of the behaviour of finite-amplitude idealised
 79 sand waves. However, migration is not considered. Fredsøe
 80 and Deigaard (1992) describe the behaviour of existing finite-
 81 amplitude dunes under a steady current. They assume the time
 82 dependence of the flow to be negligible when modelling sand
 83 waves in a tidal environment. Johns et al. (1990) discuss the
 84 finite amplitude behaviour of bed forms similar to sand waves
 85 under a steady current.

86 Numerical methods are a tool to overcome the limitations of a
 87 linear analysis and enable the study of the non-linear behaviour
 88 of these bed sand waves. This enables the description of the
 89 entire evolutionary process of sand waves and might give a clue
 90 to the most important mechanisms, determining the growth and
 91 stabilisation of sand waves. Furthermore, migration and
 92 irregular sand wave shapes can be further investigated (See
 93 Németh et al., submitted for publication).

94 Software packages like Delft3D-MOR and Telemac form
 95 promising tools for future research. However, they are

complex making it difficult to interpret the results and modify
 the model set up if necessary. Furthermore, a fully 3D
 morphological version of Delft3D-MOR (not depth-integrat-
 ed) has only become available recently. Therefore, we
 developed a new simulation model, with the specific purpose
 of simulating offshore sand waves. Herein, we only incorporat-
 ed the essential processes and focussed on the required
 accuracy to describe the vertical circulation cells responsible
 for the formation and long term evolution of offshore sand
 waves.

Within this paper, we focus on the first step, which is to
 reproduce the results obtained using a linear stability analysis
 for small amplitude sand waves Németh et al. (2002) (from
 here on referred to as “stability analysis”) with the new
 numerical simulation model (from here on referred to as
 “simulation model”). Hereby, we will focus on sand waves in a
 unidirectional steady current.

Firstly, we present the mathematical formulation of the
 sand wave simulation model. It is based on the two-
 dimensional vertical shallow water equations combined with
 a simple sediment transport equation, describing bed load
 transport. Next, the numerical set-up pursued in this work is
 discussed. We present the coordinate transformation method,
 the spatial and temporal discretisation. Subsequently, we
 validate the simulation model mathematically by comparing
 it with the linear stability analysis discussed in Németh et al.
 (2002). In the final section, we present the discussion and
 conclusions.

2. 2DV morphological model

2.1. Flow model

The simulation model presented in this paper is based on
 Németh et al. (2002). It is known that the Coriolis force only
 slightly affects sand waves Hulscher (1996). Therefore, the
 behaviour of sand waves can be described with the help of the

96
 97
 98
 99
 100
 101
 102
 103
 104
 105
 106
 107
 108
 109
 110
 111
 112
 113
 114
 115
 116
 117
 118
 119
 120
 121
 122
 123
 124
 125
 126
 127
 128
 129

130 two-dimensional vertical (2DV) model. We start from the 2DV
131 shallow water equations:

$$\frac{\partial u}{\partial t} + u \frac{\partial u}{\partial x} + w \frac{\partial u}{\partial z} = -g \frac{\partial \zeta}{\partial x} + \frac{\partial}{\partial z} \left(A_v \frac{\partial u}{\partial z} \right), \quad (1)$$

132
$$\frac{\partial u}{\partial x} + \frac{\partial w}{\partial z} = 0. \quad (2)$$

133 The symbols g and A_v indicate the acceleration due to
136 gravity and the vertical eddy viscosity, respectively. Time is
137 represented by t . The velocities in the x - and z - directions are u
138 and w , respectively. The water level is denoted by ζ and
139 H represents the mean water depth. The level of the seabed is
140 represented by $-H+h$ (see Fig. 2).

141 2.2. Sediment transport and seabed behaviour

142 The sediment transport model in this paper describes bed
143 load transport. This mode of transport is assumed to be
144 dominant in offshore tidal regimes (See also Besio and
145 Blondeaux, 2003). As the velocity distribution over the water
146 column is calculated explicitly, bed load transport can be
147 modelled as a function of the shear stress at the seabed. This is
148 in contrast with depth-averaged models, which calculate the
149 sediment transport as a function of the depth-averaged velocity.
150 The following general volumetric bed load formula for S_b is
151 used, following Komarova and Hulscher (2000):

$$S_b = \alpha |\tau_b|^b \left[\tau_b - \lambda_1 \frac{\partial h}{\partial x} - \lambda_2 |\tau_b| \frac{\partial h}{\partial x} \right], \quad (3)$$

152 with τ_b the shear stress at the seabed:

$$\tau_b = A_v \frac{\partial u}{\partial z} \Big|_{z=-H+h}. \quad (4)$$

153 The power of transport (b) is set at 1/2. The proportionality
157 constant α is set at a value of 0.3 s m^{-2} following Van Rijn
158 (1993) and incorporates the density difference between water
159 and sediment. The first scale factor for the bed slope
160 mechanism (λ_1) and the second scale factor λ_2 take directly
161 into account that sand is transported more easily downhill than
162 uphill. The default values of λ_1 and λ_2 are set at $0.002 \text{ m}^2 \text{ s}^{-2}$
163 and 3.33, respectively. In the stability analysis Németh et al.
164 (2002), λ_1 and λ_2 were taken together (i.e. $\lambda = \lambda_1 + \lambda_2 |\tau_b|_{z=-H}$)
165 since both terms in that case contribute in the same manner
166 since $h \ll NH$. In this study, a threshold of sediment motion is
167 not taken into account explicitly.

The sediment balance, which couples the flow model Eqs. 168
(1) and (2) with the sediment transport model Eq. (3), 169
calculates the position of the seabed based on the principle of 170
conservation of mass as a function of time: 171

$$\frac{\partial h}{\partial t} = -\frac{\partial S_b}{\partial x}. \quad (5)$$

The bed level will hardly vary on a tidal timescale. 172

2.3. Boundary conditions and assumptions 175

The boundary conditions at the water surface ($z=\zeta$) are 176
given as follows: 177

$$\frac{\partial \zeta}{\partial t} + u \frac{\partial \zeta}{\partial x} = w, \quad (6)$$

$$\frac{\partial u}{\partial z} = \frac{\tau_w}{A_v}. \quad (7)$$

178 in which τ_w describes the wind induced shear stress at the sea 179
surface. The vertical velocity component at the seabed 181
($z=-H+h$) is described by the kinematic condition: 182

$$\frac{\partial h}{\partial t} + u \frac{\partial h}{\partial x} = w. \quad (8)$$

The horizontal flow components at the seabed are modelled 183
with the help of a partial slip condition (S is the resistance 186
parameter controlling the resistance at the seabed). The 187
boundary condition couples the resistance at the seabed with 188
the water movement across the seabed: 189

$$A_v \frac{\partial u}{\partial z} = Su. \quad (9)$$

A comprehensive discussion on the parameter S and its 190
relation to observed bed forms can be found in Hulscher and 193
Van den Brink (2001) and Besio et al. (2004). 194

195 Furthermore, we use non-periodic boundary conditions in 196
the horizontal and vertical direction. This set up also gives 197
more freedom to the system with respect to the selection of the 198
fastest growing mode. In a periodic set up, the amount of 199
modes which can be unstable is limited by the horizontal length 200
of the grid, since we pose a limitation on the wavelength the 201
simulation model is allowed to select. Since we are also 202
interested in the behaviour of the wavelength of a sand wave 203
during its evolution, we keep the simulation model set up as 204
generic as possible.

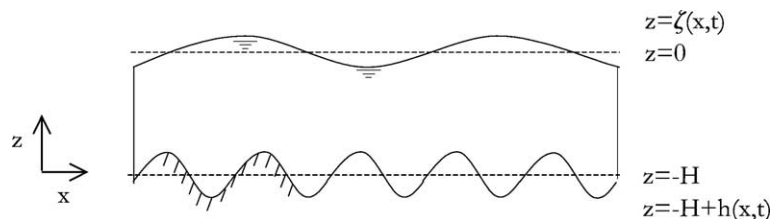


Fig. 2. Definition sketch of the non-periodic dimensional model geometry of the physical domain. The horizontal and vertical direction are denoted by x and z . The water surface is defined by ζ relative to $z=0$. The seabed is defined as h and is relative to the average seabed position, $-H$.

At the in flow boundary, a discharge is prescribed, with a certain velocity profile in the vertical plane. In case of a steady flow, two possible origins are investigated in Németh et al. (2002). These are (I) a wind driven current (τ_w) and (II) a current induced by a pressure gradient. The vertical structure for each of these cases is:

$$I: \quad u_r = \frac{\tau_w}{A_v} \left(H + \frac{A_v}{S} + z \right), \quad (10)$$

$$II: \quad u_r = P \left(\frac{1}{2} z^2 - \frac{A_v}{S} H - \frac{1}{2} H^2 \right), \quad (11)$$

with P a parameter determining the magnitude of the pressure gradient and thereby the depth-averaged velocity. These profiles are equivalent to the analytical expressions of the basic state situation over a flat seabed used in the stability analysis with the seabed positioned at $z = -H + h$. In this paper we will only focus on the effect of a wind driven current.

The outflow boundary is physically an open boundary. However, the simulation model requires a boundary condition. Therefore, an estimate of the water level is supplied to the simulation model at the outflow boundary. Furthermore, the derivatives in the horizontal direction for the horizontal and vertical velocities are set to zero at the outflow boundary.

2.4. Discussion boundary conditions

Even though we are setting up the simulation model in a non-periodic way, we investigate the possibility of applying periodic conditions. Periodic boundary conditions provide the main benefit of simplifying the system, decreasing calculation time. Since the outflow and inflow boundary are then the same, no extra physical space needs to be reserved near the boundaries, avoiding the problem of physical disturbances reaching the boundaries and reflecting.

A wind stress applied at the sea surface (Eqs. (10) and (7)) is balancing the resistance in the system equally over the entire domain. This forcing mechanism induces water movement without a gradient in the water level for a flat seabed. The water level and velocity profile at the outflow boundary are therefore the same as the inflow boundary (when the position and gradient of the seabed are the same at both boundaries). Therefore, it is also possible to use periodic boundary conditions in the horizontal direction. Obviously, the vertical direction always has to remain non-periodic.

When we apply a pressure gradient at the inflow boundary Eq. (11), the water level decreases moving away from the inflow boundary, due to resistance in the domain. Due to continuity (Eq. (2)), the depth-averaged velocity increases along the reducing water level. Therefore, the velocity profiles, water and seabed levels at the in and outflow boundary can never coincide. Tidal motion can be approached as a time-dependent pressure gradient at the inflow boundary. Therefore, in the set up of applying periodic boundary conditions, the entire tidal wave needs to be described. In practice, this is not feasible, since we require accurate results

for a relative small length scale (sand waves with a wavelength of hundreds of metres compared to the wavelength of a tidal wave of hundreds of kilometres). However, periodic boundary conditions are also here possible in the case of a pressure gradient if we incorporate the pressure gradient directly in the momentum equation Eq. (1). Then, the simulation model still contains a free surface, which responds to variations in the seabed. However, no gradient is present in the case of a flat seabed, making periodic boundary conditions possible.

3. Numerical approximation

3.1. Spatial discretisation

A spectral collocation method is used to obtain a discrete approximation of the equations of the solution, on a set of discrete grid points (Canuto et al., 1988; Fornberg, 1996). This method is applied in both coordinate directions. The discrete grid points are specified by collocation points. The grid points are given by the most commonly used Chebyshev Gauss–Lobatto points:

$$\xi^k = \cos\left(\frac{\pi j}{N}\right), \quad \text{with } j = 0, 1, \dots, N^k \quad \text{and} \quad (12)$$

$$k = 1, 3.$$

The collocation method implies that the residual function is forced to zero at these points. N^k defines the number of intervals in the ξ^k -direction. The solution is represented at each grid point using one-dimensional basis functions. The basis functions consist of the Chebyshev polynomials (T_p) defined by:

$$T_p(Z) = \cos(p \cos^{-1}(Z)), \quad \text{with } p = 1, 2, \dots \quad (13)$$

For the grid points, the Chebyshev collocation derivative can be obtained in two different ways. The first method is to calculate the derivatives in spectral space (transform method). This method involves three steps. Firstly, a Discrete Chebyshev Transform has to be applied, after which differentiation can take place in spectral space. The solution then has to be transformed back to physical space using the Inverse Discrete Chebyshev Transform.

The second method—differentiation in physical space—combines the three steps of the transform method. This results in a matrix \mathbf{D} given by Canuto et al. (1988), which can be used to calculate the first derivative at the grid points:

$$\mathbf{D}_{ij} = \begin{cases} \frac{c_i^{i+j}}{c_j x_i - x_j}, & i \neq j \\ \frac{-x_j}{2(1-x_j^2)}, & 0 < i = j < N \\ -\frac{2N^2+1}{6}, & i = j = 0 \\ \frac{2N^2+1}{6}, & i = j = N. \end{cases} \quad (14)$$

where

$$c_j = \begin{cases} 2, & j = 0 \text{ or } j = N \\ 1, & 1 \leq j \leq N - 1. \end{cases} \quad (15)$$

299 The matrix necessary to calculate a second derivative at the
 300 grid points can be calculated by taking the square of matrix **D**
 301 given in Eq. (14). The vector containing the function values *U*
 302 at the collocation points is multiplied with this first or second
 303 derivative matrix to obtain a vector containing the values for
 304 the first or second derivative values at the collocation points,
 305 respectively. The two-dimensional version of Eq. (14) in the
 306 horizontal and vertical direction can be found in the Appendix
 307 in Eqs. (40) and (41).

308 3.2. Coordinate transformation

309 A coordinate transformation is required allowing for a
 310 smooth description of the seabed topography together with a
 311 varying water surface on the computational grid. This transfor-
 312 mation will allow the total number of collocation points to
 313 remain the same irrespective of the local water depth.

314 The coordinate system used for the computational space is
 315 represented by ξ^1 for the horizontal direction and ξ^3 for the
 316 vertical direction (see also Fig. 3). Both directions of the
 317 computational coordinate system have a domain of $[-1,1]$
 318 to coincide with the Gauss–Lobatto grid. This system is
 319 obtained by mapping the physical space, represented by the
 320 Cartesian coordinates *x* and *z*, with the following analytical
 321 transformations:

$$\xi^1 = 1 - \frac{2x}{N_{sw}L_{sw}}, \quad (16)$$

$$\xi^3 = 1 - \frac{2(z - \zeta)}{\zeta + H - h}, \quad (17)$$

322
 323 with L_{sw} the initial wavelength of the sand wave chosen to be
 325 investigated with the simulation model and N_{sw} the number of
 326 sand waves in the domain. The total length of the domain is
 327 therefore N_{sw} times the wavelength L_{sw} .

328 3.3. Partial derivatives

329 Next, we compute the necessary partial derivatives for (ζ , *h*,
 330 *u*, *w*), to compensate for the changes in physical space
 331 projected on the fixed computational grid and η the computa-
 332 tional time:

$$\frac{\partial u}{\partial x} = \frac{\partial u}{\partial \xi^1} \frac{2}{N_{sw}L_{sw}} + 2 \frac{\partial u}{\partial \xi^3} \frac{\zeta_x - \frac{1}{2}(\xi^{3^2} - 1)(\zeta_x - h_x)}{\zeta + H - h}, \quad (18)$$

$$\frac{\partial u}{\partial z} = \frac{\partial u}{\partial \xi^3} \frac{2}{\zeta + H - h}, \quad (19)$$

$$\frac{\partial^2 u}{\partial z^2} = \frac{\partial^2 u}{\partial \xi^{3^2}} \left\{ \frac{2}{\zeta + H - h} \right\}^2, \quad (20)$$

$$\frac{\partial u}{\partial t} = 2 \frac{\partial u}{\partial \xi^3} \frac{\partial \zeta}{\partial t} \frac{1 - \frac{1}{2}(\xi^{3^2} - 1)}{\zeta + H - h} + \frac{\partial u}{\partial \eta}. \quad (21)$$

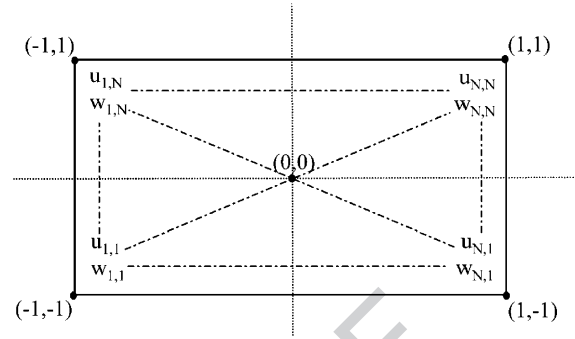


Fig. 3. Computational grid and indices used in the code.

The necessary partial derivatives for the other variables *w*, *h* and ζ can be derived in a similar manner.

3.4. Temporal discretisation flow model and grid

The spatial approximation using a Chebyshev grid is the best in the interior of the domain. Therefore, an increased density of grid points is required near the boundaries. The numerical convergence rate of the method decreases significantly if this is not the case. This aspect has an effect on the choice of the time scheme. An explicit scheme is desirable, with respect to the computational effort necessary per time step. However, the size of the time step, is determined by the smallest distance between grid points in the domain. Therefore, a higher density of grid points near the boundaries—as with the Gauss–Lobatto grid—poses a problem. If we increase the total number of grid points, the smallest distance between grid points will decrease more than the relative increase in points. The time step will become too small to be efficient.

The most practical approach is therefore to use a fully implicit formulation. In this case the time step does not depend anymore on the spatial discretisation for stability reasons. All the properties of *u*, *w*, ζ and *h* are calculated simultaneously at each time step. The calculation cost per time step is higher than for an explicit formulation. However, the time steps that can be taken are much larger (See also Stelling et al. (1998)).

The system is solved with the routine D02NGF from the Nag libraries. It is a general-purpose routine, which can integrate initial value problems, for a stiff system of ordinary differential equations, with coupled algebraic equations. The system is written in the form:

$$\mathbf{A}(t, \mathbf{Y}) \frac{d\mathbf{Y}}{dt} = \mathbf{r}(t, \mathbf{Y}), \quad (22)$$

with $\mathbf{Y}=(u, w, \zeta, h)$ the solution vector. On the left hand side, we find the derivatives of the solution vector **Y**. Matrix **A** can be found in the Appendix Eq. (42).

On the right hand side, their dependency on time can be found. Here, the differential equations and boundary conditions, which do not have a time-dependent term, appear as the residuals of the continuity equation (Eq. (2)). When the right hand side is zero, we are looking at a steady state solution. If it is non-zero, the solution is changing in time.

379 The momentum balance Eq. (1) containing the temporal
380 discretisation in the form of Eq. (22) can be written as
381 follows:

$$\begin{aligned} \frac{u}{t} = & -2 \frac{\partial \zeta}{\partial t} \frac{1 - \frac{1}{2}(\xi^3 - 1)}{\zeta + H - h} \mathbf{D}_1^3 u - \frac{2}{N_{sw} L_{sw}} u \mathbf{D}_1^1 u \\ & - 2 \frac{\zeta_x - \frac{1}{2}(\xi^3 - 1)(\zeta_x - h_x)}{\zeta + H - h} u \mathbf{D}_1^3 u + \frac{2}{\zeta + H - h} w \mathbf{D}_1^3 u \\ & - g \frac{2}{N_{sw} L_{sw}} \mathbf{D}_1^1 \zeta + A_v \frac{2}{\zeta + H - h} \mathbf{D}_2^3 u. \end{aligned}$$

382 Here \mathbf{D}_k^i is the k -th derivative in the i -th direction. The
385 partial derivatives h_x and ζ_x are of the form of Eq. (18).

386 The continuity equation (Eq. (2)) is an instantaneous
387 constraint that applies at each time level and can be found
388 on the right hand side of Eq. (22) as a time independent
389 equation:

$$\begin{aligned} \frac{2}{N_{sw} L_{sw}} \mathbf{D}_1^1 u + 2 \frac{\zeta_x - \frac{1}{2}(\xi^3 - 1)(\zeta_x - h_x)}{\zeta + H - h} \mathbf{D}_1^3 u \\ - \frac{2}{\zeta + H - h} \mathbf{D}_1^3 w = 0. \end{aligned} \quad (24)$$

390 At the in flow boundary Eqs. (10) and (11) we find:

$$u = \text{prescribed}|_{x=-1} \quad \text{and} \quad w = 0|_{x=-1}. \quad (25)$$

393 At the outflow boundary, we find the horizontal derivatives
396 of u and w set to zero, resulting in:

$$\frac{2}{N_{sw} L_{sw}} \mathbf{D}_1^1 u + 2 \frac{\zeta_x - \frac{1}{2}(\xi^3 - 1)(\zeta_x - h_x)}{\zeta + H - h} \mathbf{D}_1^3 u = 0|_{x=1}, \quad (26)$$

$$\frac{2}{N_{sw} L_{sw}} \mathbf{D}_1^1 w + 2 \frac{\zeta_x - \frac{1}{2}(\xi^3 - 1)(\zeta_x - h_x)}{\zeta + H - h} \mathbf{D}_1^3 w = 0|_{x=1}. \quad (27)$$

397 Furthermore, the water level is fixed at the downstream
399 boundary. The boundary condition at the free surface can now
401 be written as a kinematic condition Eq. (6), together with a
402 shear stress at the surface equal to the wind stress Eq. (7)
403 (if present):
404

$$\frac{\partial \zeta}{\partial \eta} + u \frac{2}{N_{sw} L_{sw}} \mathbf{D}_1^3 \zeta = w|_{z=\zeta}, \quad (28)$$

$$- \frac{2}{\zeta + H - h} \mathbf{D}_1^3 = \tau_w|_{z=\zeta}. \quad (29)$$

405 At the seabed we find another kinematic condition Eq. (8)
408 and the partial slip condition Eq. (9):
409

$$w - u \frac{2}{N_{sw} L_{sw}} \mathbf{D}_1^1 h = 0|_{z=-H+h}, \quad (30)$$

$$u - \frac{2}{\zeta + H - h} \frac{A_v}{S} \mathbf{D}_1^3 u = 0|_{z=-H+h}. \quad (31)$$

The sediment transport model Eq. (3) in discretised form
can be written as:

$$\begin{aligned} S_b = & \alpha \left(\frac{2}{\zeta + H - h} \right)^2 \mathbf{D}_1^3 |u|^b \\ & \left[\mathbf{D}_1^1 u - (\lambda_1 + \lambda_2 |\tau_b|) \frac{\zeta + H - h}{N_{sw} L_{sw}} \mathbf{D}_1^1 h \right], \end{aligned} \quad (32)$$

with τ_b the shear stress at the seabed defined by Eq. (4). The
net inflow of sediment is assumed to be zero. The seabed
evolution Eq. (5) can now be described on the computational
grid by:

$$\frac{\partial h}{\partial t} = \frac{2}{N_{sw} L_{sw}} \mathbf{D}_1^1 S_b. \quad (33)$$

For completeness, we have to specify a boundary condition
at a boundary coinciding with the horizontal position of the
flow boundaries for the bottom evolution equation. This is
equivalent to the boundary condition necessary for the water
level. This can also be done by taking the derivative of the
sediment transport equal to zero coinciding with a fixed
seabed. At this point, only the initial response is needed here
for comparison with the results from the stability analysis.

3.5. Initial values and time stepping

For a flat seabed, the initial conditions can be derived
analytically. In case the seabed is not flat, but contains for
example a sinusoidal feature, we cannot use the solution for a
flat seabed. However, we can use it as an estimate for the
required initial condition. A better initial condition can be
given by the solution of the stability analysis, which is valid for
infinitesimal amplitudes ($h \ll H$) Németh et al. (2002).

The estimates of the initial solution prescribed using these
two approaches for a finite sinusoidal sand wave are not the
exact solutions of the system. This difference in applied
solution and the actual solution can be seen as an initial
disturbance in the system. The order of magnitude of the error/
disturbance depends on the ratio of h/H , the spatial discretisa-
tion and the requested accuracy from the time integrator.

The propagation velocity c of a wave in shallow water is
calculated with:

$$c = \sqrt{gH} \quad (34)$$

A steady state solution, which we in general require to start
a simulation, can be achieved by letting the disturbances travel
through the domain a couple of times. For a typical water depth
of 30 m, the propagation velocity is about 17 m s⁻¹ according
to Eq. (34). For a domain with a length of 2 km, this would
mean that a disturbance in the water motion due to the incorrect
initial solution takes about 120 s to travel from one end of the
domain to the other. After about 600 s we can expect a virtually
steady state solution. This solution can then form the starting
point for a simulation.

In the limit ($t \rightarrow \infty$) the changes in time for a steady state
solution should be equal to zero. Therefore, the residuals of Eq.

461 (22) are practically zero which is discussed below. Further-
 462 more, this aspect can be seen by looking at the magnitude of
 463 the time step of the time integrator. This time step is small
 464 initially due to the calculation of all the dependencies of the
 465 system and possible initial changes in the physical system.
 466 Large time steps can be taken when the steady state situation
 467 has been attained, as long as the seabed does not change.

468 When the seabed is allowed to change, the magnitude of the
 469 time step becomes a function of this seabed change. The time
 470 steps are then still large due to the slow evolution of the seabed
 471 compared to the water movement, in case of a steady state
 472 current. This is due to the difference in timescale for the water
 473 motion and seabed change. This only holds for the case of a
 474 steady current or a block current. In the case of pure tidal
 475 motion, the time step size is again determined by the timescale
 476 of the water motion. However, here we will first investigate if
 477 we can reproduce the initial response of applying a seabed
 478 perturbation using a simulation model.

479 4. Results

480 We start with the investigation of a steady flow. First, we
 481 discuss in short this steady flow and its effects on the behaviour
 482 of the seabed with the help of a stability analysis. The steady
 483 flow is assumed to be induced by a wind stress applied at the
 484 sea surface. Next, we show that the results from the simulation
 485 model coincide with the stability analysis.

486 4.1. Steady flow and sand waves according to a stability 487 analysis

488 We start by focussing on a unidirectional steady current
 489 inducing the initial evolution of bed forms. The bed forms we
 490 find in this case can also be referred to as dunes [Fredsoe and
 491 Deigaard, 1992], since a unidirectional steady current is similar
 492 to river flow. For typical values of the resistance parameter S
 493 in the North Sea (see Table 1), we find long wavelengths (see
 494 Fig. 4). Hereby, we used in the stability analysis a combined
 495 non-dimensional value for λ_1 and λ_2 (Eq. (3)):

$$S_b = \alpha |\tau_b|^b \left[\tau_b - \lambda \frac{\partial h}{\partial x} \right] \quad \text{with } \lambda = \lambda_1 - \lambda_2 |\tau_b|, \quad (35)$$

496 with λ equal to 0.0085. However, if we increase the value of
 497 the resistance parameter, we find shorter bed forms Németh et
 498 al. (2001) (See Figs. 4 and 6. The latter figure is discussed later
 499 in more detail.), with wavelengths of a couple of hundreds of
 500 metres. This coincides with the result found in Németh et al.
 501 (2002). In a tidal environment with a small asymmetry in the
 502 water motion, the tidal motion is the main factor determining
 503 the choice of sand wavelength. The residual currents due to
 504 tidal motion induce a wider range of modes which can become
 505 unstable than the unidirectional steady current. An increase in
 506 resistance can increase this range of modes, for which the
 507 wavelength of the fastest growing mode (FGM) is smaller
 508 (larger wave number). Here, the FGM is the mode which has
 509 the largest growth rate from linear theory, and is expected to
 510 dominate over the rest.

Table 1

Default values and dimensions of the parameters and variables existing in the system

Parameters	Symbol	Default value	Dimension
Depth-averaged value velocity	U	1	m s^{-1}
Average water depth	H	30	m
Kinematic eddy viscosity	A_v	$3 \cdot 10^{-2}$	$\text{m}^2 \text{s}^{-1}$
Resistance parameter	S	$1 \cdot 10^{-2}$	m s^{-1}
Gravitational acceleration	g	9.8	m s^{-2}
Power of transport	b	$5 \cdot 10^{-1}$	–
Proportionality constant	α	$3 \cdot 10^{-1}$	$\text{m}^{-2} \text{s}$
Bed slope factor	λ_1	$2 \cdot 10^{-3}$	$\text{m}^2 \text{s}^{-2}$
Bed slope factor	λ_2	3.33	–
Sand wavelength	L_{sw}	600	m
Number of sand waves	N_{sw}	3	–

4.2. Mathematical validation simulation model

4.2.1. Flat bed

We start with a steady current over a flat bed, which is equivalent to the basic state used in the stability analysis. We apply a wind stress at the sea surface (see Eq. (10) and Fig. 5) across a flat seabed together with a coinciding in flow boundary. The analytically obtained profile is the same over the entire domain. This investigation of a flat seabed shows the functionality of the continuity equation (Eq. (2)), the boundary conditions Eqs. (6)–(11) and the viscosity term in the momentum equation Eq. (1).

We investigate the magnitude of the residuals on the right hand side of Eq. (22), whether the solution coincides with the solution of the physical system. Since the solution provided is a steady state solution and the velocity in the vertical is zero (there is no slope in the seabed or water level), all the residuals on the right hand side of Eq. (22) should be zero within machine accuracy limits. The profile in the vertical can be found in Fig. 5.

If we would apply a pressure gradient at the inflow boundary, a gradient is present in the water surface due to the friction in the system. This is in contrast to the stability analysis, where the velocity profile is the same over the entire domain. This makes a direct comparison more difficult. However, this can also be seen as a good test for the simulation model and the usage of the basic state in the stability analysis.

We can take an initial condition for a flat seabed and an equal velocity profile over the entire domain equal to inflow boundary for a pressure gradient Eq. (11). If we fix the water level downstream ($z=0$) and fix the depth-averaged velocity at the inflow boundary, we obtain a steady state solution with a slope in the water level. The continuity equation enforces the depth-averaged velocity to increase along this decreasing slope. This slope decreases $8.45 \cdot 10^{-3}$ m per 10 km for a standard value of the resistance parameter S of $1 \cdot 10^{-3} \text{ m s}^{-1}$ (see Table 1). In case we are looking at bed forms in a unidirectional steady current, the typical value for S is $1 \cdot 10^{-2} \text{ m s}^{-1}$ and gives a slightly larger slope of $1.46 \cdot 10^{-2}$ m per 10 km. This slope is so small compared to the length scale under investigation, that we can assume the validity as expected of the basic state used in the stability analysis.

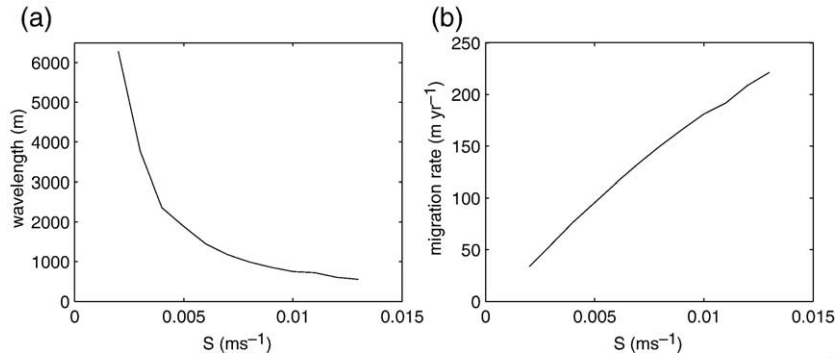


Fig. 4. Wavelength and migration rate in a unidirectional steady current induced by a wind stress applied at the sea surface. Fig. (a) shows the wavelength (m) of the fastest growing mode (FGM) as a function of the value of the resistance parameter S (m s^{-1}). Fig. (b) shows the migration rate in metres of the FGM shown in (a). If we increase the value of the resistance parameter S we obtain sand waves with dimensions in the order of hundreds of metres.

553 4.2.2. Residuals solution for small amplitude sand waves

554 The question to be answered is whether the formation process
 555 of small amplitude sand waves can be reproduced and verified
 556 with a simulation model. To check this we use the results
 557 obtained with the stability analysis. The vertical velocity is zero
 558 for a flat bed situation. The vertical velocity to be imported in the
 559 simulation model is equal to the calculated vertical velocity in
 560 the perturbed state in the stability analysis. The sum of the
 561 residual horizontal velocity and the basic state forms the actual
 562 horizontal velocity with sand waves applied on the seabed.
 563 These results, produced on an equidistant grid, are interpolated
 564 on the Gauss–Lobatto grid, using cardinal polynomials.

565 The time derivative is equivalent to the residuals in Eq. (22).
 566 For the other equations, the magnitude of the residuals, is a
 567 measure for the error. To check the validity of the spatial
 568 discretisation, we therefore do not need to use the time
 569 integrator. The results for a wavelength of 600 m are imported
 570 in the simulation model (See Fig. 6). The solution of the
 571 stability analysis is multiplied by $\epsilon = h/H$. For a small enough
 572 ϵ , the solution from the simulation model is equal to the
 573 solution from the stability analysis (residuals equal zero within
 574 numerical accuracy, with a difference of the order (ϵ^2).

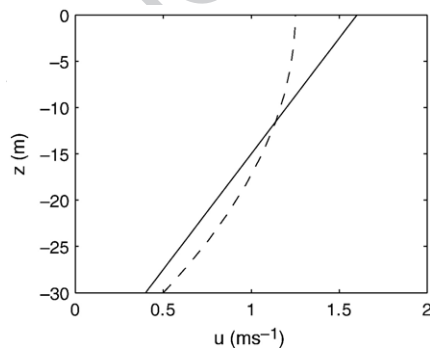


Fig. 5. Analytical solution of the horizontal velocity profile over a flat bed in case of a wind stress applied at the sea surface (straight solid line) Eq. (10) and a pressure gradient (curved dotted line) Eq. (11). The linearity of the velocity profile in case of a wind stress is due to the choice of a constant viscosity. The free surface coincides with $z = 0$ m and the seabed with $z = -30$ m. The vertical velocity is equal to zero. This profile is applied at the inflow boundary for all times (with a fixed or time-dependent discharge) and as initial condition over the entire domain.

4.2.3. Growth and migration

As a final check, we allowed the simulation model to determine a seabed change over a period of 7000 s. This is a small time interval, insignificant from a morphological perspective. However, from a mathematical point of view sufficient, since the aim is here to check the mathematical validity of the simulation model. We applied again a steady flow induced by a wind stress. With the system set up following the values in Table 1, except for the value of the resistance parameter which is equal to 0.01 m s^{-1} . Furthermore, we used the same combined bed slope factor as was used above (Eq. (3)) for comparison. Moreover, we took $N^1 = 30$ and $N^3 = 15$, which are the number of grid points in the horizontal and vertical direction (Eq. (12)), respectively. The amplitude h is set at 0.01 m, which is small compared to the water depth H of 30 m. Hereby, we investigated a pattern of three sand waves in a non-periodic domain.

We calculated the growth and migration rates, for a whole range of wavelengths. We use a least squares method, to estimate the growth and migration rates based on the initial and calculated seabed obtained with the simulation model. This curve fitting process is used to fit a sinus with a minimal deviation to the position of the seabed, with sinusoidal sand waves imprinted on it, in the grid points. Here we investigate the initial response. Therefore, we are allowed to assume the wavelength does not change, and only the amplitude and position in the horizontal (phase/migration) changes. This approach gives an estimate of the amplitude and phase of a sinusoidal signal, in this case the sand wave. This coincides with the properties the stability analysis gives insight into (growth and migration of a sinusoidal sand wave), which we are comparing the results with. These properties of the imposed sand waves and resulting bed pattern after the simulation period can now be determined as follows:

$$h(x) = A_{1s} \cos(kx) + B_{1s} \sin(kx), \quad (36)$$

with $h(x)$ the position of the seabed as a function of the horizontal coordinate and φ the phase shift defined by:

$$\varphi = \text{atan} \left(\frac{B_{1s}}{A_{1s}} \right), \quad (37)$$

575

576

577

578

579

580

581

582

583

584

585

586

587

588

589

590

591

592

593

594

595

596

597

598

599

600

601

602

603

604

605

606

607

608

609

610

611

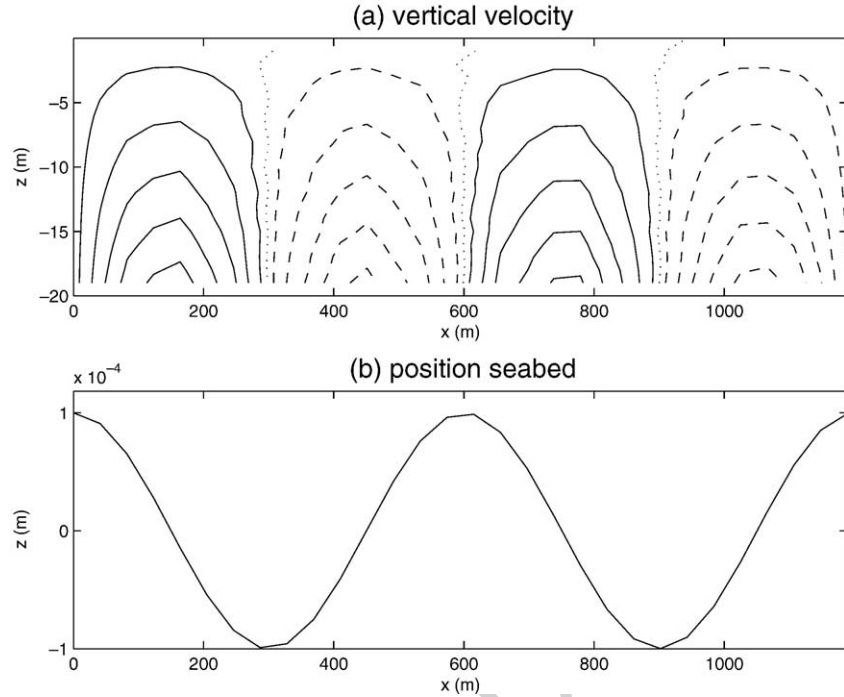


Fig. 6. Solution of the stability analysis giving residuals equal to zero in the simulation model. In the upper figure (a), the vertical velocity is shown with the solid line showing negative, the dashed line positive and the dotted line velocities equal to zero. The magnitude of the velocities depends on the ratio of the sand wave amplitude over the water depth ($\epsilon=h/H$). The vertical velocity looks different from previous work discussing sand waves in a tidal environment. The main difference is that we are looking here at a steady current and not at the residuals over a tidal cycle. This means looking at the boundary condition for the horizontal flow Eq. (8), that the vertical velocity needs to follow the profile of the seabed. This is due to the occurrence of a horizontal velocity $\neq 0$, due to the horizontal viscosity model enabling long bed waves to be excited (there is evolution due to water movement, and the slope effect is very small for long bed forms). The figure below (b) shows the two sand waves with a typical wavelength of 600 m over which the water is flowing.

613 and A and B based on the depths at the grid points:

$$A_{ls} = \frac{\sum h(x)\cos(kx)}{\sum \cos^2(kx)}, \quad (38)$$

$$B_{ls} = \frac{\sum h(x)\sin(kx)}{\sum \sin^2(kx)}. \quad (39)$$

614

615 Fig. 7 shows the characteristics of the initial response for a
618 range of wavelengths. Fig. 7a depicts the growth rates,
619 whereby we find a range of wavelengths for which these
620 growth rates are positive. For this range, sand waves are

initially unstable. Furthermore, we find for all long bed waves
positive growth rates. This is due to the usage of a constant
viscosity. It can be explained by looking at the boundary
conditions showing that the vertical velocity at the seabed is a
function of the horizontal velocity at the seabed (Eqs. (8) and
(9)). Both the horizontal and vertical velocity are therefore not
equal to zero. This is due to the usage of a resistance parameter
to obtain a more realistic shear stress with this simplified
viscosity model. Smaller wavelengths than about 400 m show
negative growth rates. These bed forms are damped by the
simulation model, as coincides with the results for this case
with the stability analysis. Here, the FGM has a wavelength of

621
622
623
624
625
626
627
628
629
630
631
632

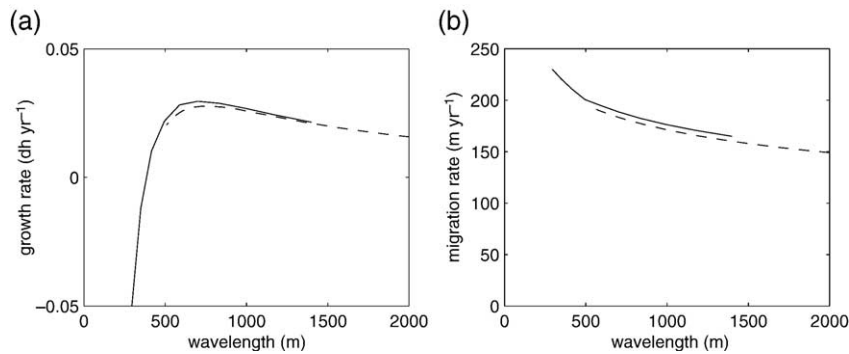


Fig. 7. Comparison growth and migration rates of the stability analysis and simulation model. Fig. (a) shows the initial growth rate presented in the change of amplitude per year ($m\ yr^{-1}$). Here we have to keep in mind that the growth rate is, according to the stability analysis, an exponential function of the amplitude. This means that the growth rate will increase during the initial evolution of a sand wave. The solid line depicts the results from the simulation model. The dotted line corresponds to the results from the stability analysis. Fig. (b) shows the migration rate (initial response calculated in $m\ yr^{-1}$).

731 to determine derivatives in the vertical direction can be written
 732 as the elements of \mathbf{D}^3 in a diagonal pattern with a spacing of N^1
 733 elements as follows:

$$\mathbf{D}^3 = \begin{pmatrix} \mathbf{D}_{11}^3 & 0 & \mathbf{D}_{12}^3 & 0 & \mathbf{D}_{1N}^3 & 0 \\ 0 & \mathbf{D}_{11}^3 & 0 & \mathbf{D}_{1j}^3 & 0 & \mathbf{D}_{1N}^3 \\ \mathbf{D}_{i1}^3 & 0 & \mathbf{D}_{ij}^3 & 0 & \mathbf{D}_{iN}^3 & 0 \\ 0 & \mathbf{D}_{i1}^3 & 0 & \mathbf{D}_{ij}^3 & 0 & \mathbf{D}_{iN}^3 \\ \mathbf{D}_{N1}^3 & 0 & \mathbf{D}_{Nj}^3 & 0 & \mathbf{D}_{NN}^3 & 0 \\ 0 & \mathbf{D}_{N1}^3 & 0 & \mathbf{D}_{Nj}^3 & 0 & \mathbf{D}_{NN}^3 \end{pmatrix} \quad (41)$$

736 The rest of the elements are zero.

737 The matrix below with a total size of $N^1 \times N^3 \times 2 + N^1 \times 2$
 738 can be found in Eq. (22) and consist of the variables depending
 739 on time in the momentum equation Eq. (1) (the first $N^1 \times N^3$
 740 rows), the continuity equation (Eq. (2)) giving elements equal
 741 to zero (the next $N^1 \times N^3$ rows), and the equation for the water
 742 level Eq. (6) and the bed evolution Eq. (8) ($2 \times N^1$ rows). For
 743 the water level, we use the kinematic boundary condition at the
 744 free surface. This is equivalent to using a depth-averaged
 745 formulation based on the continuity equation and this
 746 kinematic boundary condition often used to describe a free
 747 surface:

$$A = \begin{pmatrix} \frac{\partial u}{\partial t} & 0 & f\left(\frac{\partial \zeta}{\partial t}\right) & f\left(\frac{\partial h}{\partial t}\right) \\ 0 & 0 & 0 & 0 \\ 0 & 0 & \frac{\partial \zeta}{\partial t} & 0 \\ 0 & 0 & 0 & \frac{\partial h}{\partial t} \end{pmatrix} \quad (42)$$

748 See Eq. (23) for the numerical notation.

751 **References**

752
 753 Allen, J.R.L., 1980a. Sand waves: a model of origin and internal structure.
 754 Sediment. Geol. 26, 281–328.
 755 Allen, J.R.L., 1980b. Sand wave immobility and the internal master bedding of
 756 sand wave deposits. Geol. Mag. 117 (5), 347–446.
 757 Besio, G., Blondeaux, P., 2003. On the effect of the suspended load on the
 758 formation of sand waves. In: Snchez-Arcilla, A., Bateman, A. (Eds.),
 759 RCEM 2003, Proceedings Third IAHR Symposium on River, Coastal and
 760 Estuarine Morphodynamics. Spain, IHAR, Madrid, pp. 365–375.
 761 Besio, G., Blondeaux, P., Brocchini, M., Vittori, G., 2003. Migrating sand
 762 waves. Ocean Dyn. 53, 232–238.
 763 Besio, G., Blondeaux, P., Brocchini, M., Vittori, G., 2004. On the modeling
 764 of sand wave migration. J. Geophys. Res. 109, C04018, doi:10.1029/
 765 2002JC001622.
 766 Canuto, C., Quarneroni, A., Yousuff Hussaini, M., 1988. Spectral Methods in
 767 Fluid Dynamics. ISBN: 0-387-17371-4.
 768 Fornberg, B., 1996. A Practical Guide to Pseudospectral Methods, Cambridge
 769 Monographs on Applied and Computational Mathematics, vol. 1. Univer-
 770 sity of Colorado, Cambridge University Press.

Fredsøe, J., Deigaard, R., 1992. Mechanics of Coastal Sediment Transport, 771
 Institute of Hydrodynamics and Hydraulic Engineering. Technical Univer- 772
 sity of Denmark, pp. 260–289. 773
 Gerkema, T., 2000. A linear stability analysis of tidally generated sand waves. 774
 J. Fluid Mech. 417, 303–322. 775
 Hulscher, S.J.M.H., 1996. Tidal induced large-scale regular bed form patterns 776
 in a three dimensional shallow water model. J. Geophys. Res. 101 (C9), 777
 20727–20744. 778
 Hulscher, S.J.M.H., Van den Brink, G.M., 2001. Comparison between 779
 predicted and observed sand waves and sandbanks in the North Sea. J. 780
 Geophys. Res. 106 (C5), 9327–9338. 781
 Huthnance, J., 1982. On one mechanism forming linear sandbanks. Estuar. 782
 Coast. Shelf Sci. 14, 79–99. 783
 Johns, B., Soulsby, R.L., Chesher, T.J., 1990. The modelling of sand wave 784
 evolution resulting from suspended and bed load transport of sediment. 785
 J. Hydraul. Res. 28 (3), 355–374. 786
 Johnson, M.A., Stride, A.H., Belderson, R.H., Kenyon, N.H., 1981. Predicted 787
 sand-wave formation and decay on a large offshore tidal-current sand-sheet. 788
 Spec. Publ. Int. Assoc. Sedimentol. 5, 247–256. 789
 Knaapen, M.A.F., Hulscher, S.J.M.H., 2002. Regeneration of dredged sand 790
 waves. Coast. Eng. 46 (4), 277–289. 791
 Komarova, N.L., Hulscher, S.J.M.H., 2000. Linear instability mechanisms for 792
 sand wave formation. J. Fluid Mech. 413, 219–246. 793
 Komarova, N.L., Newell, A.C., 2000. Non-linear dynamics of sandbanks and 794
 sand waves. J. Fluid Mech. 415, 285–321. 795
 Lanckneus, J., De Moor, G., 1991. Present-day Evolution of Sand Waves on a 796
 Sandy Shelf Bank, Oceanologica Acta, Proceedings of the International 797
 Colloquium on the Environment of Epicontinental seas, Lille, sp vol. 11, 798
 pp. 123–127. 799
 Langhorne, D.N., 1981. An evaluation of Bagnolds dimensionless coefficient 800
 of proportionality using measurements of sand wave movements. Mar. 801
 Geol. 43, 49–64. 802
 Morelissen, R., Hulscher, S.J.M.H., Knaapen, M.A.F., N’emeth, A.A., Bijker, 803
 R., 2003. Interacting sand waves and pipelines: a data-assimilation based 804
 mathematical model. Coast. Eng. 48 (3), 197–209. 805
 N’emeth, A.A., Hulscher, S.J.M.H., Van Damme, R.M.J., 2001. Numerical 806
 simulation of sand wave evolution in shallow shelf seas. In: Hanson, H., 807
 Larson, M. (Eds.), Proceedings of the Fourth Conference on Coastal 808
 Dynamics, Lund, Sweden, pp. 1048–1057. 809
 N’emeth, A.A., Hulscher, S.J.M.H., de Vriend, H.J., 2002. Modelling sand 810
 wave migration in shallow shelf seas. Cont. Shelf Res. 22 (18–19), 811
 2795–2806. 812
 A.A. N’emeth, S.J.M.H. Hulscher, R.M.J. Van Damme, 2004. Modelling 813
 offshore sand wave evolution. submitted for publication. 814
 Peters, B.G.T.M., Hulscher, S.J.M.H., Roos, P.C., 2001. Large-scale sand 815
 extraction offshore: interacting between model and decision process. 816
 FOMAR.-Congreso Internacional Ciencia Y Tecnologia Marina, April 817
 24–27th, Spain. 818
 Stelling, G., Roose, D., Sommeijer, B.P., Houwen, P.J., Kok, J., Lin, H.X., Tan, 819
 K., 1998. New generation shelf flux models. Modelling, Analysis and 820
 Simulation (MAS) MAS-R9815. Report MAS-R9815. CWI, The Nether- 821
 lands p. 32. 822
 Stolk, A., 2000. The role of sandwaves in the management of the Netherlands 823
 Continental Shelf. In: Trentesaux, A., Garlan, T. (Eds.), Marine Sandwave 824
 Dynamics, International Workshop, March 23–24 2000, University of Lille 825
 1, France, Proceedings, pp. 93–197. 826
 Van Maren, D.S., 1998. Sand Waves, A State-of-the-Art Review and 827
 Bibliography. North Sea Directorate, Ministry of Transport, Public Works 828
 and Water Management, The Netherlands. 118 pp. 829
 Van Rijn, L.C., 1993. Handbook of sediment transport by currents and waves. 830
 Delft Hydraulics, Delft, The Netherlands. 831